

This is a copy of the published version, or version of record, available on the publisher's website. This version does not track changes, errata, or withdrawals on the publisher's site.

Current-driven insulator-to-metal transition without Mott breakdown in Ca_2RuO_4

Davide Curcio, Charlotte E. Sanders, Alla Chikina, Henriette E. Lund, Marco Bianchi, Veronica Granata, Marco Cannavacciuolo, Giuseppe Cuono, Carmine Autieri, Filomena Forte, Guerino Avallone, Alfonso Romano, Mario Cuoco, Pavel Dudin, Jose Avila, Craig Polley, Thiagarajan Balasubramanian, Rosalba Fittipaldi, Antonio Vecchione, and Philip Hofmann











Published version information:

Citation: Curcio (et.al) Current-driven insulator-to-metal transition without Mott breakdown in Ca_2RuO_4 , PHYSICAL REVIEW B108, L161105(2023)

DOI: <https://doi.org/10.1103/PhysRevB.108.L161105>

This version is made available in accordance with publisher policies. Please cite only the published version using the reference above. This is the citation assigned by the publisher at the time of issuing the APV. Please check the publisher's website for any updates.

Current-driven insulator-to-metal transition without Mott breakdown in Ca_2RuO_4

Davide Curcio ¹, Charlotte E. Sanders,² Alla Chikina,¹ Henriette E. Lund,¹ Marco Bianchi,¹ Veronica Granata ³, Marco Cannavacciuolo ³, Giuseppe Cuono ⁴, Carmine Autieri ⁴, Filomena Forte,⁵ Guerino Avallone,³ Alfonso Romano,³ Mario Cuoco ⁵, Pavel Dudin,⁶ Jose Avila,⁶ Craig Polley,⁷ Thiagarajan Balasubramanian ⁷, Rosalba Fittipaldi ⁵, Antonio Vecchione ⁵ and Philip Hofmann ^{1,*}

¹Department of Physics and Astronomy, Aarhus University, DK-8000 Aarhus C, Denmark

²Central Laser Facility, STFC Rutherford Appleton Laboratory, Harwell OX11 0QX, United Kingdom


³Dipartimento di Fisica “E. R. Caianiello,” Università degli Studi di Salerno, via Giovanni Paolo II 132, I-84084 Fisciano (Sa), Italy

⁴International Research Centre Magtop, Institute of Physics, Polish Academy of Sciences, Aleja Lotników 32/46, PL-02668 Warsaw, Poland

⁵CNR-SPIN, via Giovanni Paolo II 132, I-84084 Fisciano, Italy

⁶Synchrotron SOLEIL, FR-91192 Gif-sur-Yvette, France

⁷MAX IV Laboratory, Lund University, SE-211 00 Lund, Sweden

 (Received 13 February 2023; revised 9 June 2023; accepted 2 October 2023; published 16 October 2023)

The electrical control of a material’s conductivity is at the heart of modern electronics. Conventionally, this control is achieved by tuning the density of mobile charge carriers. A completely different approach is possible in Mott insulators such as Ca_2RuO_4 , where an insulator-to-metal transition (IMT) can be induced by a weak electric field or current. While the driving force of the IMT is poorly understood, it has been thought to be a breakdown of the Mott state. Using *in operando* angle-resolved photoemission spectroscopy, we show that this is not the case: The current-induced conductivity is caused by the formation of in-gap states with only a minor reorganization of the Mott state. Electronic structure calculations show that these in-gap states form at the boundaries of structural domains that emerge during the IMT. At such boundaries, the overall gap is drastically reduced, even if the structural difference between the domains is small and the individual domains retain their Mott character. The inhomogeneity of the sample is thus key to understanding the IMT, as it leads to a nonequilibrium semimetallic state that forms at the interface of Mott domains.

DOI: [10.1103/PhysRevB.108.L161105](https://doi.org/10.1103/PhysRevB.108.L161105)

An electrical current can be expected to trigger an insulator-to-metal transition (IMT) in many correlated oxides, since Joule heating can push the local temperature high enough for a temperature-induced transition to take place [1]. However, in some materials, the IMT can be triggered by surprisingly low-current densities, and the effect is thought to be mainly electronic [2].

A particularly well-established example is Ca_2RuO_4 , a Mott insulator with a complex phase diagram and a strong susceptibility to phase changes that can be triggered not only by electric fields and currents [3–5], but also by temperature [6,7], pressure [8], doping [9,10], and strain [11]. The current-induced IMT in this system has been investigated using a large variety of tools. While the results are not generally consistent, owing to the complexity of the phase diagram and the still disputed role of Joule heating [12–15], there are several established experimental facts: (1) The transition’s fingerprint is a region of negative differential resistance in transport measurements [4,5,12,16]; (2) macroscopically, the transition proceeds across the sample starting from the negative electrode [12,15]; and (3) the IMT is strongly coupled to a structural phase transition involving an expansion of the crystal’s *c* axis: Starting from the so-called “*S* phase,” with

a short *c* axis [17], a fully metallic “*L* phase” emerges, with a significant *c*-axis expansion. Diffraction techniques confirm the trend of *c*-axis expansion, accompanied by the simultaneous presence of different structural phases [16,18–21]. Joule heating might play a role in creating some of these [20].

Manifestly absent from the experimental results are direct characterisations of the electronic structure in the current-induced phase. Such information can, in principle, be obtained from angle-resolved photoemission spectroscopy (ARPES), but the application of photoemission techniques is hindered by a simple experimental limitation: In a current-carrying sample, the voltage drop inside the sample area illuminated by the ultraviolet (UV) light spot for photoemission is sufficiently large to completely deteriorate the energy resolution of the experiment. Here, we solve this problem by using a very small light spot, on the order of a few μm , allowing us to characterize the electronic structure throughout the IMT. In addition to spectroscopic information, this approach gives access to the local potential landscape on the surface, and we can thus use it as a local transport measurement [22,23].

ARPES experiments were carried out at the ANTARES beamline of the SOLEIL synchrotron facility [24]. The setup of the experiment is shown in Fig. 1(a). The Ca_2RuO_4 sample [25] is cleaved *in situ* parallel to the *ab* plane while electrically contacted from the sides, so that both the electronic structure and the current-induced potential landscape can be mapped

*philip@phys.au.dk

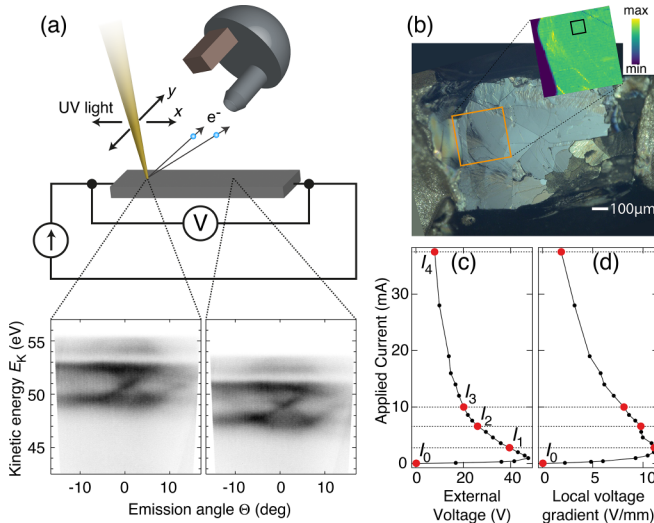


FIG. 1. (a) Sketch of the experiment. The current-induced voltage drop results in local photoemission spectra that are displaced in energy, following the local potential landscape across the sample. (b) Optical microscope image of the sample. The contacts are seen on the left- and right-hand side. The area explored by ARPES is marked by an orange square. The inset shows a map of the photoemission intensity inside this area. (c) Externally measured I/V curve and (d) local I/V curve obtained from averaging the observed energy shift between the spectra within the black square marked in the inset of (b) [26]. The red markers indicate the current values for which data are displayed in Figs. 2 and 3.

by the scanning of a highly focused UV beam ($3.6 \mu\text{m}$) across the sample surface. When this is done as a function of the applied current, it results in a five-dimensional data set: the photoemission intensity as a function of the spatial coordinates x and y , kinetic energy E_k , emission angle Θ , and the current I . The sample temperature is held constant at 200 K. Two local photoemission spectra (photoemission intensity as a function of E_k and Θ) are given as examples. Due to the presence of the electric field accompanying the current density, the spectra collected at different points are displaced in energy. Figure 1(b) shows an optical microscopy image of the sample. The current-dependent electronic structure has been studied in the area outlined by the orange square. The inset of Fig. 1(b) shows a map of the integrated photoemission intensity in this region, with intensity changes that clearly correspond to the sample's microscopic morphology. For more experimental details, see Supplemental Material (SM) [26], including Ref. [27].

Figure 1(c) shows the macroscopic I/V curve, obtained from the applied current and the voltage drop across the entire sample. This is compared to a local I/V curve [Fig. 1(d)] derived from the potential gradient measured by ARPES (see SM) [22,26]. Both show the shape typical for the current-induced IMT, with a pronounced region of negative differential resistance [4,5,12,16]. Note that the local I/V curve is equivalent to a genuine four-point measurement and is thereby different from the external measurement, which includes the sample's contact resistance. A comparison of the curves requires the assumption that the ratio of total current and the current through the area probed by the local

measurement is independent of the magnitude of the total current. The similarity of the two I/V curves shows that the local spectroscopic measurements reported here are representative of a sample area undergoing the IMT.

Photoemission spectra across the IMT are given in Fig. 2 as measurements of the photoemission intensity throughout the Brillouin zone for the equilibrium situation and three selected currents; (for additional data, see SM [26]). The zero current I_0 and even the low-current spectrum at I_1 agree very well with published equilibrium results [11,28,29]. The two flat bands at low binding energies (marked by arrows) are related to the d_{xz} and d_{yz} states of the Ru-4d t_{2g} manifold. In the insulating S phase, these are half filled, and are a manifestation of the lower Hubbard band in a Mott state driven by Coulomb interactions [28]. The remaining d_{xy} band is fully occupied, and thus insulating. It gives rise to the circular intensity feature marked by arrows in Figs. 2(a) and 2(b) [26]. The more intense bands at a higher binding energy are primarily derived from oxygen states.

The IMT to a conducting L phase is predicted to result in a breakdown of the Mott state, i.e., in a proper metallic state with a large Fermi surface [18,30]. Clearly, this is at odds with the ARPES results, which show an absence of Fermi level crossings at the higher currents I_2 and I_4 (see Fig. 2). Indeed, an increased current only results in minor changes of the spectra. The signature of the Mott state remains and the most prominent effect appears to be a mere k broadening that washes out the dispersive features. This is particularly evident in the oxygen bands, but it also takes place in the Ru states. The broadening can either signal that k_{\parallel} ceases to be a good quantum number, possibly because of the creation of defects or small crystalline domains, or it can point towards the simultaneous existence of structural domains with slightly different electronic structures, such that their incoherent superposition is observed here [26]. Both mechanisms are consistent with the observation of a broad distribution of structural modifications in diffraction experiments [16,18–21] (see SM for x-ray diffraction results from the crystals used here [26]). The persistence of the Mott state in all of these structural modifications is a key result of this Letter.

An important question is to what degree spectral intensity is filled into the Mott gap, triggering the transition in conductivity. In equilibrium, the Fermi energy E_F is constant throughout the system. It can be measured precisely from the sample's metal contacts and then the intensity at E_F can be mapped. In the presence of a current this is not possible because of energy displacement of the spectra—and hence also of the local E_F —across the sample, as illustrated in Fig. 1(a). In order to determine this *local* Fermi energy, we find a nondispersive feature in the spectra and measure its binding energy with respect to E_F in equilibrium. Assuming that this binding energy remains the same when a current is applied allows us to reconstruct the local E_F throughout the current-carrying sample.

In detail, we proceed as follows: We first reduce the complexity of the spectra, by integrating each of them along the emission angle, resulting in angle-integrated energy distribution curves (EDCs), as shown in Figs. 2(i)–2(l). The integration in angle is justified by the very small dispersion observed in the $\{d_{xz}, d_{yz}\}$ bands. Each EDC is fitted by two

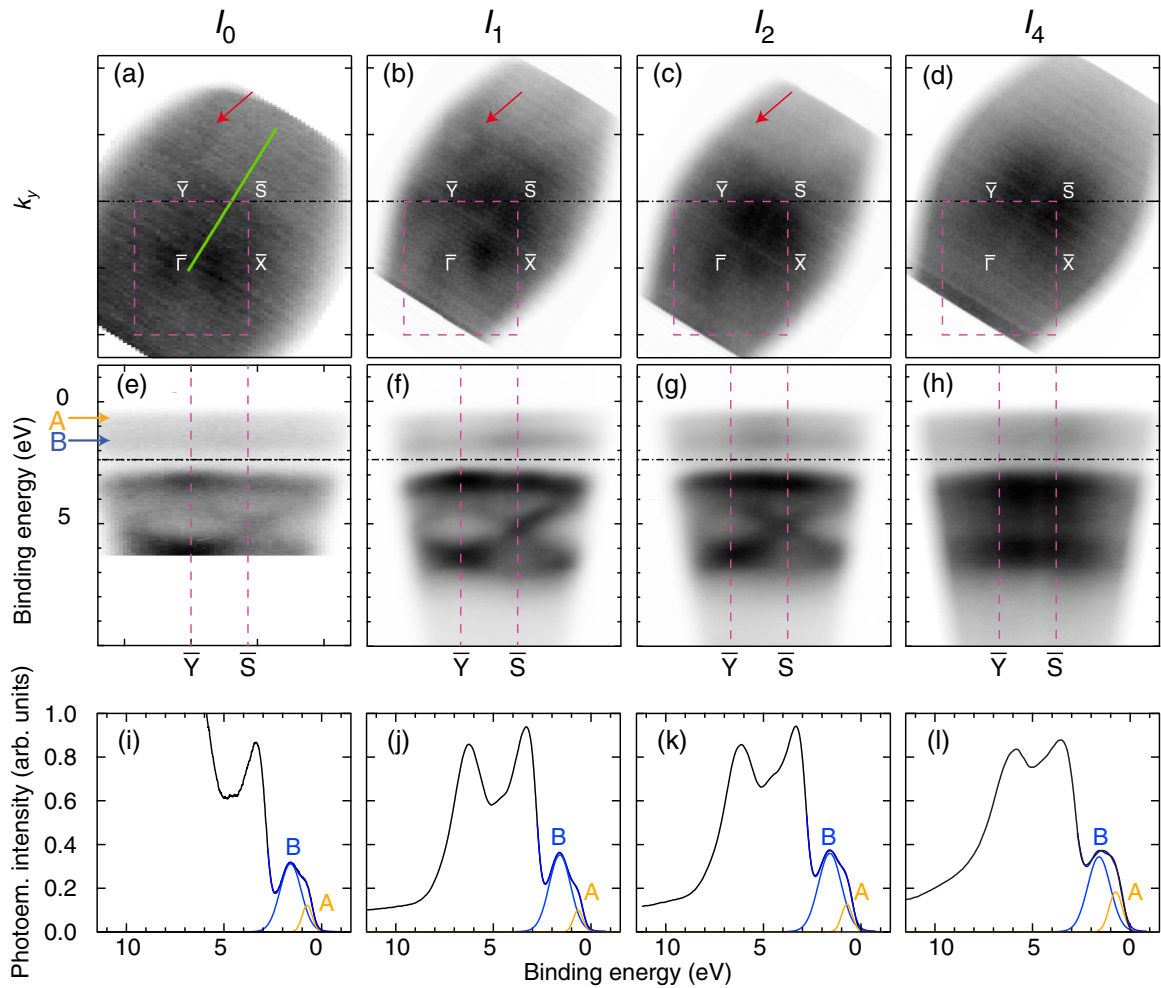


FIG. 2. Photoemission spectra across the IMT: (a)–(d) Photoemission intensity at a binding energy of 2.37 eV for I_0 , I_1 , I_2 , I_4 [see markers in Fig. 1(c)]. The surface Brillouin zone is superimposed. The green line marks the direction and range of the spectra in Fig. 3. The red arrow marks a circular constant energy contour stemming from the d_{xy} states. (e)–(h) Intensity as a function of energy along the $\bar{Y}\bar{S}$ direction. (i)–(l) Angle-integrated energy distribution curves for no current and the three currents, integrated along the green line in (a). The photoemission intensity at low binding energy has been fitted by two peaks, A and B, in the same way as in Ref. [28]. The peak positions are also marked in (i)–(l).

Voigt peaks in the $\{d_{zx}, d_{yz}\}$ energy region, called A and B [28]. These fits are also shown in Figs. 2(i)–2(l). We then choose the B peak as a common energy reference point. The A peak is clearly unsuitable because it is closest to the gap where spectral changes are expected. The B peak appears to be a good choice for two reasons: (1) It represents a flat band in the equilibrium state; and (2) in contrast to the A peak, it is only weakly affected by the corresponding strain-induced IMT [11]. The zero-current binding energy of the B peak is 1.60 eV, measured against a Fermi edge of polycrystalline Au. Combining this with the local energy from the fit, we obtain the local E_F and thus a binding energy scale for every spectrum. The spectra in Fig. 2 are already plotted using this scale (for details, see SM [26]).

Following this procedure, we can now plot the in-gap spectral intensity as the integrated intensity around the local E_F for maps of the current-carrying sample [see Fig. 3(a)]. As expected, the in-gap intensity increases with the current throughout the sample. Moreover, the buildup of in-gap intensity initiates at the negative electrode (on the left-hand side),

consistent with the optical observation of the phase transition [12,15]. This is clearly seen by the yellow edge developing on the left-hand side of the sample in Fig. 3(a) in the panel for I_2 . This spreads from left to right across the image as seen for I_3 , eventually covering the entire sample at I_4 . Figure 3(b) shows the spectral development at a selected point in the maps [marked with a white box in Fig. 3(a)], and Fig. 3(c) gives the corresponding integrated EDCs in the region of the A and B peaks. The evolution is consistent with that in Fig. 2 and the increase of spectral weight in the gap, while small, can be observed in the EDCs. The increased spectral weight also correlates with the estimated current density and local conductivity. Indeed, a clear increase of the local conductivity starts at the turning point of the I/V curve, as expected (see Fig. S2 in the SM [26]).

The appearance of in-gap states can explain the onset of the IMT in the sample's conductivity, even if it appears to be at odds with the conventional picture of an IMT resulting from a Mott breakdown. However, it raises questions about the possible origin of the in-gap states. A potentially important element

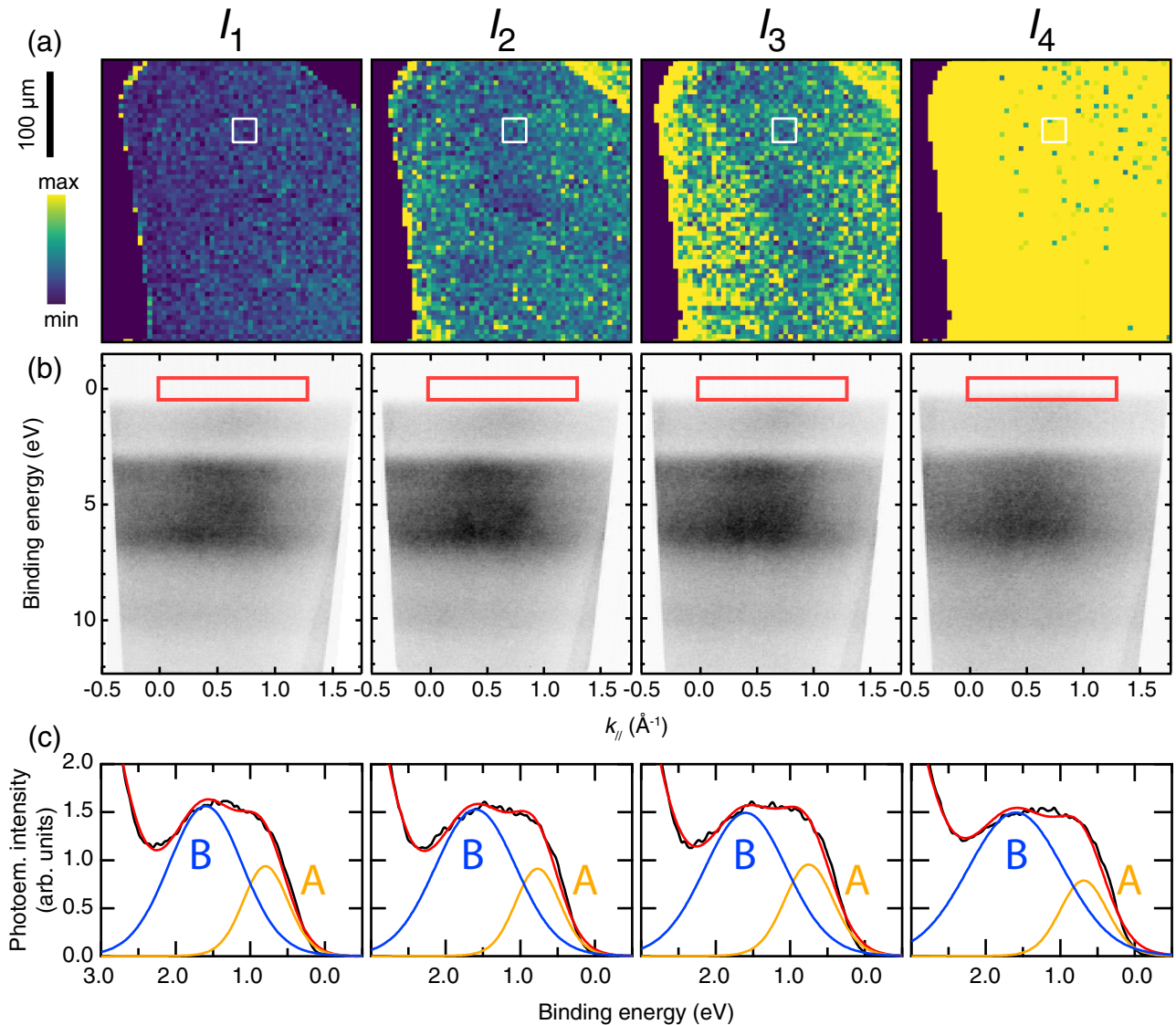


FIG. 3. Mapping the IMT throughout the data set. (a) In-gap photoemission intensity across the sample for selected currents marked in Fig. 1(c). The integration region is given by the red rectangles in (b). (b) Corresponding photoemission spectra at the location marked by a white rectangles in (a). (c) Angle-integrated energy distribution curves obtained from the spectra in (b).

missing in calculations modeling the IMT [11,18,30–32] is structural inhomogeneity which is clearly present according to diffraction experiments [16,18–21]. We show that this inhomogeneity can indeed explain the presence of states in the bulk band gap. These arise at the interface between different structural domains.

We consider a simple model in which Ca_2RuO_4 structural units with a slightly different c -axis parameter are interfaced with each other. To this end, Fig. 4(a) compares the electronic density of states (DOS) for the equilibrium S phase and a modified S' phase with a small (3%) expansion of the c axis (calculated by density function theory [31,33–39]; for details, see SM [26]). The influence of the structural change is very small. Both phases are insulating with a very similar gap and the features mainly appear shifted in energy [26]. This shift, however, is crucial as it results in an effective band gap between the valence band maximum of the S phase and the conduction band minimum of the S' phase that is drastically

reduced compared to the gap in either of the pure phases. This smaller gap would be present at the interface between the two phases, creating electronic states lying inside the bulk band gap of a homogeneous phase. The reason for the relative energy shift is the strong covalency of the Ru $4d$ states combined with a distance variation between the Ru and the apical oxygen atoms that is changing the crystal field. As expected, the oxygen states are also affected by the modified interaction with the Ru atoms (see Fig. 2 and SM [26]).

While a single interface between the S and S' phases already captures the creation of interfacial in-gap states, a more appropriate model for the experimental situation might be, for example, a superlattice with alternating S and S' phases, i.e., “flat” and “not-so-flat” octahedra. Such a structure is sketched in Fig. 4(b), constructed such that S and S' layers are stacked with a layer of intermediate structure in between. The calculated DOS for this superlattice is also shown in Fig. 4(b). Now the distinction between the contributions of the

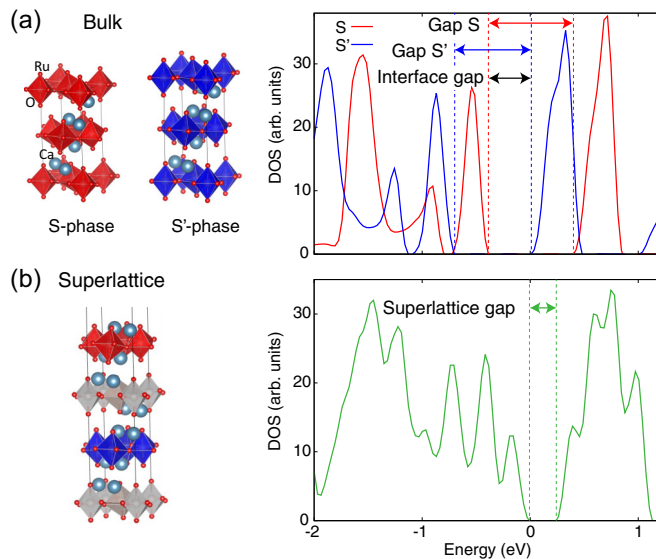


FIG. 4. (a) Sketch of the Ca_2RuO_4 bulk crystal structures and corresponding density of states (DOS). S and S' have unit cells with a different c -axis lengths. S and S' are insulating with the indicated gaps but the band alignment leads to a smaller effective gap at the interface between S and S' . (b) Superlattice formed by the S and S' unit cells separated by an interface unit cell with intermediate properties (gray octahedra). The corresponding DOS shows a substantial reduction of the charge gap. The zero of the energy scale is fixed to the valence band maximum of the superlattice throughout this Letter.

individual phases loses meaning, but a reduced gap manifests itself directly in the overall DOS. The gap reduction is qualitatively similar for other choices of the superlattice (see SM [26]). The experimental situation is presumably more complicated than this, with inhomogeneous domain sizes that give rise to a continuum of energetically displaced and slightly different band structures. This will further increase the tendency to form in-gap states, in excellent qualitative agreement with the ARPES results. We stress that all this proceeds without destroying the local Mott state, and that the resulting phase can be viewed as an emergent inhomogeneous band-Mott semimetallic state. Such a state can retain the high-energy

features of the Coulomb-driven insulator while allowing for an in-gap spectral weight and a conductivity increase due to the current-driven structural inhomogeneities.

In conclusion, we have shown that the current-driven IMT in Ca_2RuO_4 leads to the expected increase of in-gap spectral weight, but that the Mott state appears to be largely retained. An emergent semimetallic state with simultaneous Mott character can be explained by the current-induced structural inhomogeneity of the sample, because the band alignment between structurally different domains effectively reduces the overall gap. Our work thus unveils a nonequilibrium semimetallic state that forms at the interface of Mott domains. In contrast to what would be expected on the basis of well-known mechanisms, this situation arises from the structural inhomogeneity of a system, and it is entirely different than the mere coexistence of insulating and metallic domains that would be expected for a first-order phase transition. The creation of a different phase from microstructuring has not been reported in connection with the IMT in transition metal oxides, but it is somewhat reminiscent of the hidden phase in laser- or current-exposed $1T\text{-TaS}_2$ [40], where metallicity is induced in a modified Mott phase by nanotexturing [41].

Note added in proof. It has come to our attention that results on the IMT of Ca_2RuO_4 using a similar approach are reported in [42].

This work was supported by VILLUM FONDEN via the Centre of Excellence for Dirac Materials (Grant No. 11744). G.C. and C.A. are supported by the Foundation for Polish Science through the International Research Agendas program co-financed by the European Union within the Smart Growth Operational Programme (Grant No. MAB/2017/1). G.C. and C.A. acknowledge the access to the computing facilities of the Interdisciplinary Center of Modeling at the University of Warsaw, Grants No. G84-0, No. GB84-1, and No. GB84-7. We acknowledge SOLEIL for provision of synchrotron radiation facilities and MAX IV Laboratory for time on Beamline Bloch under Proposal No. 20190681. Research conducted at MAX IV, a Swedish national user facility, is supported by the Swedish Research council under Contract No. 2018-07152, the Swedish Governmental Agency for Innovation Systems under Contract No. 2018-04969, and Formas under Contract No. 2019-02496.

[1] Z. Shao, X. Cao, H. Luo, and P. Jin, *NPG Asia Mater.* **10**, 581 (2018).
 [2] G. Cao, *J. Phys.: Condens. Matter* **32**, 423001 (2020).
 [3] F. Nakamura, M. Sakaki, Y. Yamanaka, S. Tamaru, T. Suzuki, and Y. Maeno, *Sci. Rep.* **3**, 2536 (2013).
 [4] R. Okazaki, Y. Nishina, Y. Yasui, F. Nakamura, T. Suzuki, and I. Terasaki, *J. Phys. Soc. Jpn.* **82**, 103702 (2013).
 [5] M. Sakaki, N. Nakajima, F. Nakamura, Y. Tezuka, and T. Suzuki, *J. Phys. Soc. Jpn.* **82**, 093707 (2013).
 [6] C. S. Alexander, G. Cao, V. Dobrosavljevic, S. McCall, J. E. Crow, E. Lochner, and R. P. Guertin, *Phys. Rev. B* **60**, R8422(R) (1999).

[7] J. H. Jung, Z. Fang, J. P. He, Y. Kaneko, Y. Okimoto, and Y. Tokura, *Phys. Rev. Lett.* **91**, 056403 (2003).
 [8] F. Nakamura, T. Goko, M. Ito, T. Fujita, S. Nakatsuji, H. Fukazawa, Y. Maeno, P. Alireza, D. Forsythe, and S. R. Julian, *Phys. Rev. B* **65**, 220402(R) (2002).
 [9] S. Nakatsuji and Y. Maeno, *Phys. Rev. Lett.* **84**, 2666 (2000).
 [10] T. Miyashita, H. Iwasawa, T. Yoshikawa, S. Ozawa, H. Oda, T. Muro, H. Ogura, T. Sakami, F. Nakamura, and A. Ino, *Solid State Commun.* **326**, 114180 (2021).
 [11] S. Riccò, M. Kim, A. Tamai, S. McKeown Walker, F. Y. Bruno, I. Cucchi, E. Cappelli, C. Besnard, T. K. Kim, P. Dudin *et al.*, *Nat. Commun.* **9**, 4535 (2018).

- [12] J. Zhang, A. S. McLeod, Q. Han, X. Chen, H. A. Bechtel, Z. Yao, S. N. Gilbert Corder, T. Ciavatti, T. H. Tao, M. Aronson, G. L. Carr, M. C. Martin, C. Sow, S. Yonezawa, F. Nakamura, I. Terasaki, D. N. Basov, A. J. Millis, Y. Maeno, and M. Liu, *Phys. Rev. X* **9**, 011032 (2019).
- [13] K. Fürsich, J. Bertinshaw, P. Butler, M. Krautloher, M. Minola, and B. Keimer, *Phys. Rev. B* **100**, 081101(R) (2019).
- [14] G. Mattoni, S. Yonezawa, F. Nakamura, and Y. Maeno, *Phys. Rev. Mater.* **4**, 114414 (2020).
- [15] G. Chiriacò and A. J. Millis, *Phys. Rev. B* **102**, 085116 (2020).
- [16] C. Cirillo, V. Granata, G. Avallone, R. Fittipaldi, C. Attanasio, A. Avella, and A. Vecchione, *Phys. Rev. B* **100**, 235142 (2019).
- [17] O. Friedt, M. Braden, G. André, P. Adelmann, S. Nakatsuji, and Y. Maeno, *Phys. Rev. B* **63**, 174432 (2001).
- [18] J. Bertinshaw, N. Gurung, P. Jorba, H. Liu, M. Schmid, D. T. Mantadakis, M. Daghofer, M. Krautloher, A. Jain, G. H. Ryu *et al.*, *Phys. Rev. Lett.* **123**, 137204 (2019).
- [19] H. Zhao, B. Hu, F. Ye, C. Hoffmann, I. Kimchi, and G. Cao, *Phys. Rev. B* **100**, 241104 (2019).
- [20] K. Jenni, F. Wirth, K. Dietrich, L. Berger, Y. Sidis, S. Kunkemöller, C. P. Grams, D. I. Khomskii, J. Hemberger, and M. Braden, *Phys. Rev. Mater.* **4**, 085001 (2020).
- [21] R. Okazaki, K. Kobayashi, R. Kumai, H. Nakao, Y. Murakami, F. Nakamura, H. Taniguchi, and I. Terasaki, *J. Phys. Soc. Jpn.* **89**, 044710 (2020).
- [22] D. Curcio, A. J. H. Jones, R. Muzzio, K. Volckaert, D. Biswas, C. E. Sanders, P. Dudin, C. Cacho, S. Singh, K. Watanabe, T. Taniguchi, J. A. Miwa, J. Katoch, S. Ulstrup, and P. Hofmann, *Phys. Rev. Lett.* **125**, 236403 (2020).
- [23] P. Hofmann, *AVS Quantum Sci.* **3**, 021101 (2021).
- [24] J. Avila, I. Rizado-Colambo, S. Lorcy, B. Lagarde, J.-L. Giorgetta, F. Polack, and M. C. Asensio, *J. Phys.: Conf. Ser.* **425**, 192023 (2013).
- [25] V. Granata, R. Fittipaldi, A. Guarino, A. Ubaldini, E. Carleschi, A. M. Strydom, F. Chiarella, and A. Vecchione, *J. Alloys Compd.* **832**, 154890 (2020).
- [26] See Supplemental Material at <http://link.aps.org/supplemental/10.1103/PhysRevB.108.L161105> for experimental and theoretical details, x-ray diffraction data, additional transport and photoemission data from SOLEIL and MAX IV, and supplemental calculations of the superlattice electronic structure and density of states.
- [27] G. Avallone, R. Fermin, K. Lahabi, V. Granata, R. Fittipaldi, C. Cirillo, C. Attanasio, A. Vecchione, and J. Aarts, *npj Quantum Mater.* **6**, 91 (2021).
- [28] D. Sutter, C. G. Fatuzzo, S. Moser, M. Kim, R. Fittipaldi, A. Vecchione, V. Granata, Y. Sassa, F. Cossalter, G. Gatti *et al.*, *Nat. Commun.* **8**, 15176 (2017).
- [29] T. Mizokawa, L. H. Tjeng, G. A. Sawatzky, G. Ghiringhelli, O. Tjernberg, N. B. Brookes, H. Fukazawa, S. Nakatsuji, and Y. Maeno, *Phys. Rev. Lett.* **87**, 077202 (2001).
- [30] F. Petocchi, V. Christiansson, and P. Werner, *Phys. Rev. B* **104**, 195146 (2021).
- [31] E. Gorelov, M. Karolak, T. O. Wehling, F. Lechermann, A. I. Lichtenstein, and E. Pavarini, *Phys. Rev. Lett.* **104**, 226401 (2010).
- [32] Q. Han and A. Millis, *Phys. Rev. Lett.* **121**, 067601 (2018).
- [33] G. Kresse and J. Hafner, *Phys. Rev. B* **47**, 558 (1993).
- [34] G. Kresse and J. Furthmüller, *Comput. Mater. Sci.* **6**, 15 (1996).
- [35] G. Kresse and J. Furthmüller, *Phys. Rev. B* **54**, 11169 (1996).
- [36] G. Kresse and D. Joubert, *Phys. Rev. B* **59**, 1758 (1999).
- [37] J. P. Perdew, A. Ruzsinszky, G. I. Csonka, O. A. Vydrov, G. E. Scuseria, L. A. Constantin, X. Zhou, and K. Burke, *Phys. Rev. Lett.* **100**, 136406 (2008).
- [38] C. Autieri, *J. Phys.: Condens. Matter* **28**, 426004 (2016).
- [39] L. Vaugier, H. Jiang, and S. Biermann, *Phys. Rev. B* **86**, 165105 (2012).
- [40] L. Stojchevska, I. Vaskivskiy, T. Mertelj, P. Kusar, D. Svetin, S. Brazovskii, and D. Mihailovic, *Science* **344**, 177 (2014).
- [41] D. Cho, S. Cheon, K.-S. Kim, S.-H. Lee, Y.-H. Cho, S.-W. Cheong, and H. W. Yeom, *Nat. Commun.* **7**, 10453 (2016).
- [42] C. T. Suen, I. Marković, M. Zonno, S. Zhdanovich, N.-H. Jo, M. Schmid, P. Hansmann, P. Puphal, K. Fürsich, V. Zimmerman *et al.*, [arXiv:2308.05803](https://arxiv.org/abs/2308.05803).